Materials Science-Poland
Volume 43 Issue 3 · pp. 50–63 · DOI: 10.2478/msp-2025-0029

Materials Science-Poland

Microstructural analysis of freeze–thaw degradation in rubber-modified cement-stabilized crushed stone using X-ray computed tomography

Research Article

Shuai Mao[1,2], Yongqing Lin[3], Zurun Yue[2]*

[1] School of Traffic and Transportation, Shijiazhuang Tiedao University, Shijiazhuang, China
[2] State Key Laboratory of Mechanical Behavior and System Safety of Traffic Engineering Structures, Shijiazhuang Tiedao University, Shijiazhuang, China
[3] Beijing Jiaotong Vocational Technical College, Beijing, China

Received 10 July 2025; Accepted 01 September 2025

Abstract: This study investigates the microstructural mechanisms governing the freeze–thaw (F–T) degradation of cement-stabilized crushed stone modified with recycled rubber powder. Specimens with rubber contents of 0, 10, 20, 30, and 45% by volume of fine aggregate were evaluated. Frost resistance exhibited a non-monotonic relationship: It initially decreased at low rubber contents before increasing significantly at higher contents. To explain this, we employed high-resolution X-ray computed tomography to analyze the internal pore structure evolution. We introduce a novel metric, the pore orderliness expansion index (POEI), derived from the spatial correlation of damage between progressive F–T stages. A strong, statistically significant positive correlation was found between the POEI and frost resistance. High POEI values, indicating an orderly expansion of existing pores, corresponded to superior durability, whereas low POEI values signified disordered microcrack propagation and poor performance. The findings clarify that high rubber concentrations enhance frost resistance not merely by adding ductility but by promoting a more benign, orderly pore expansion mechanism, thereby inhibiting the formation of new, damage-inducing microcracks.

Keywords: *Cement-stabilized crushed stone • Rubber powder • Freeze–thaw cycle • Frost resistance • X-ray computed tomography • Microstructure • Pore orderliness expansion index • Waste tire recycling*

1. Introduction

The disposal of waste tires presents a significant global environmental challenge [1]. For instance, recent data from China, the world's largest tire producer, indicate the generation of approximately 330 million waste tires annually, making the development of sustainable recycling solutions imperative [2]. One of the most promising approaches is incorporating processed tire rubber into construction materials, which effectively transforms a waste product into a valuable resource [3].

In civil infrastructure, particularly for high-speed railway subgrades in seasonal frozen regions, cement-stabilized crushed stone (CSCS) is widely used to mitigate frost heave [4], as it provides necessary strength and stability [5]. However, its inherent brittleness makes it susceptible to damage from repeated freeze–thaw (F–T) cycles [6]. This can lead to significant strength loss and a reduced service life, a phenomenon investigated by researchers like Jie et al., who studied the material's deformability [7]. Specific research by Jie et al. demonstrated that unconfined compressive strength decreases as F–T cycles increase, with the most significant degradation often occurring within the initial cycles [8].

One proposed method to enhance the durability of CSCS is the inclusion of rubber powder, which can improve toughness [9]. While previous research has shown that adding rubber powder can improve frost resistance coefficient (BDR) [5], this benefit typically comes at the cost of reduced compressive strength, as documented by Jie et al. [9]. However, the underlying mechanisms

* E-mail: YuezRunZ@163.com

Open Access. © 2025 Shuai Mao *et al.*, published by Sciendo
This work is licensed under the Creative Commons Attribution-NonCommercial-NoDerivs 4.0 License.

governing these trade-offs, particularly at the microstructural level [10], remain poorly understood, and results can be inconsistent [11]. Recent studies have continued to explore these properties, but a clear consensus on the ideal rubber content and the reasons for its non-monotonic effect on durability is lacking [12].

Recent advancements in non-destructive testing [13], especially X-ray computed tomography (CT) [14], allow for the three-dimensional (3D) visualization and quantification of a material's internal structure [15]. This technology provides a powerful tool to bridge the gap between macroscopic mechanical behavior and its microstructural origins [11]. Sun et al. [14] and Huang et al. [16] have demonstrated the utility of CT scanning in analyzing mesostructure and pore characteristics in cementitious materials under various environmental cycles. While previous studies have documented the macroscopic effects of rubber, the underlying microstructural dynamics of damage remain poorly quantified. It is unclear whether improved durability at high rubber contents stems from simple ductility enhancement or a more fundamental change in the damage propagation mode. A deeper mechanistic understanding is critically important, as it allows for a shift from an empirical, "trial-and-error" approach to a more fundamental, mechanism-driven material design philosophy.

We hypothesize that superior BDR is directly linked to the spatial regularity of the pore network's expansion. To test this, this study employs high-resolution X-ray CT to visualize damage accumulation and introduces a novel metric, the pore orderliness expansion index (POEI), to quantitatively link the orderliness of micro-damage to the material's macroscopic BDR.

2. Materials and methods

2.1 Raw materials and specimen preparation

The raw materials used in this study were ordinary Portland cement, crushed limestone aggregate, and waste tire rubber powder.

Parameter type	Test value (%)	Limit (%)
Los Angeles attrition rate (>1.7 mm)	21.4	≤30
Plasticity index (<0.5 mm)	4.8	<6
Loss rate of sodium sulfate solution	5.6	≤6

Table 1. Basic parameters of crushed stone.

Square hole screen aperture (mm)	45	31.5	22.4	7.1	1.7	0.5	0.1
Percentage of screen mass	100	91	79	58	30	19	0

Table 2. CSCS sample particle size gradation (C5P0.1).

Cement: P.O 42.5 ordinary Portland cement, produced by Shijiazhuang Quzhai Cement Co., Ltd., was used. Its initial and final setting times were 150 and 240 min, respectively.

Aggregate: The aggregate was produced by crushing quarried limestone. Its fundamental properties are detailed in Table 1.

Rubber powder: Waste tire rubber powder with a relative density of 1.13 was supplied by Hebei Kexu Building Materials Co., Ltd. It was prepared by mixing five distinct particle sizes – 12, 20, 40, 60, and 80 mesh – in equal proportions by volume (1:1:1:1:1).

The mineral gradation for the CSCS was determined according to the "Code for Design of High-Speed Railway" (TB 10621-2014) [17,18]. The resulting gradation was well-graded with a coefficient of uniformity (Cu) greater than 15 (Table 2), and the cement content was set at 5% by weight of the dry aggregate.

Rubber powder was incorporated by replacing the fine aggregate fraction (particles <1.7 mm) at replacement levels of 10, 20, 30, and 45% by equal volume. Based on the material densities, these volumetric levels correspond to 1.29, 2.62, 4.0, and 6.17% of the total specimen mass, respectively. A control mixture (C5R0) with 0% rubber was also prepared. The water-to-cement ratio was maintained at 0.40 for all mixtures.

Standard cylindrical specimens (Φ150 mm × 150 mm) were fabricated using a YAW-2000 microcomputer-controlled electro-hydraulic servo pressure testing machine via static compaction to achieve a 97% compaction degree. Specimens were cured for 28 days in a standard curing room at a temperature of 20 ± 2°C and a relative humidity of ≥95%. For clarity, specimens are denoted as C5R0, C5R10, C5R20, C5R30, and C5R45, where the number indicates the rubber powder's volumetric replacement percentage of the fine aggregate.

2.2 Test methods

2.2.1 Unconfined compressive strength test

Specimens were tested for unconfined compressive strength after 7 and 28 days of curing, following water immersion. A



Figure 1. Flow chart of unconfined compressive strength test: (a) sample preparation, (b) sample curing, (c) sample soaking, and (d) unconfined compressive strength test.

WAW-300 pressure testing machine was used in accordance with standard procedures outlined in JTG E51-2009 (Figure 1).

2.2.2 BDR test

After 28 days of curing and subsequent water immersion, specimens were subjected to up to 30 F–T cycles in a programmable high- and low-temperature chamber. Each 24-h cycle consisted of 12 h at −20°C followed by 12 h at +20°C. The durability was evaluated using the BDR, calculated as

$$BDR = R_D/R_C \times 100\%, \quad (1)$$

where R_D is the unconfined compressive strength after F–T cycles, and R_C is the initial 28-day strength.

2.2.3 CT scanning and image analysis

For microstructural analysis, smaller cylindrical cores (Φ50 mm × 50 mm) were extracted from the center of the large, 28-day cured specimens, as shown in Figure 2. Care was taken to minimize damage during coring by using a low-speed, water-cooled diamond drill bit. To further mitigate any potential artifacts from the coring process, all subsequent image analyses were performed on a central region of interest within each sample, avoiding the outer edges.

Scans were performed on these cored specimens before F–T cycling (0 cycles) and then again after 5 and 10 cycles using an industrial CT scanner with parameters detailed in Table 3. The raw CT data were reconstructed into a series of 8-bit grayscale image slices [19–21]. These images were processed using Avizo software to segment the distinct material phases.

Equipment parameters	Specific range and values
Maximum sample size	Φ50 mm
Scanning voltage	150 kV
Current	60 μA
Exposure time	0.55 s
Voxel resolution	30 μm/pixel

Table 3. X-ray CT equipment parameters.

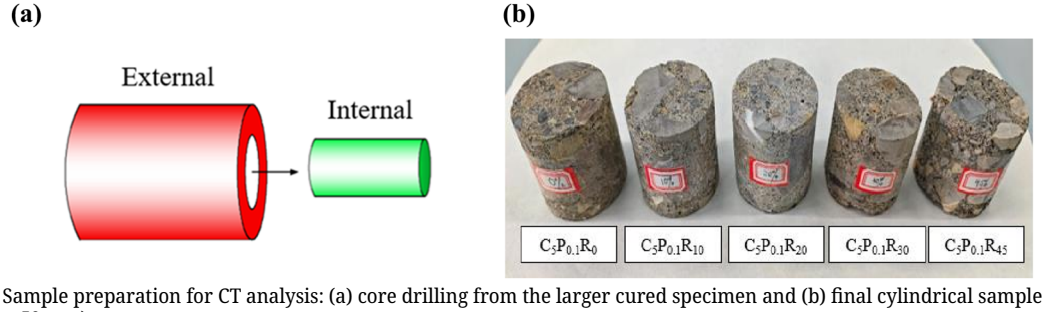

Figure 2. Sample preparation for CT analysis: (a) core drilling from the larger cured specimen and (b) final cylindrical sample (Φ50 mm × 50 mm).

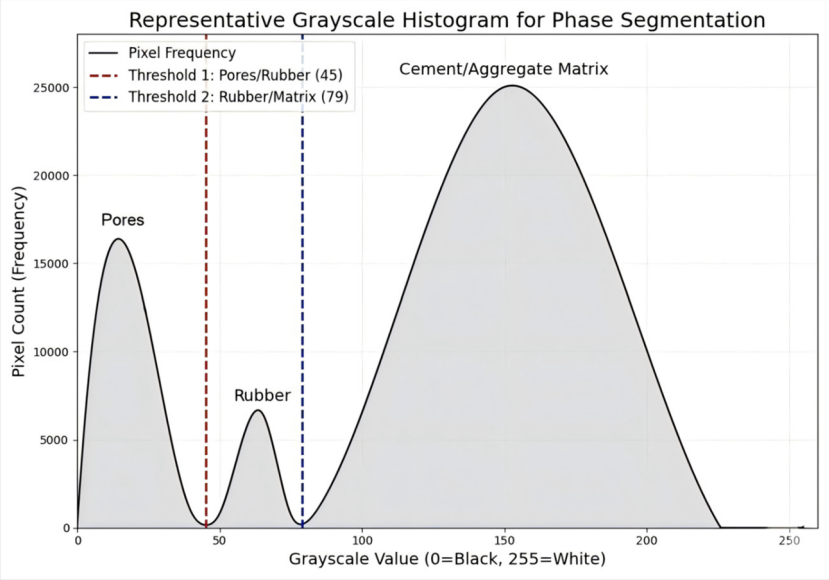

Figure 3. Representative grayscale histogram used for phase segmentation.

To establish objective and repeatable segmentation criteria, a grayscale histogram analysis was performed on the reconstructed images. As shown in the representative histogram in Figure 3, the material exhibits a clear multi-modal distribution, with three distinct peaks corresponding to the primary phases. The first peak, at low grayscale values (approximately 25), corresponds to the pores (air voids). The second peak (approximately 65) represents the rubber powder, and the third, and largest, peak (approximately 150) corresponds to the dense cement/aggregate matrix. The thresholds for segmentation were determined by identifying the valleys (local minima) between these peaks, which represent the grayscale values least likely to be shared between phases. This analysis confirmed that the optimal threshold between pores and rubber powder was at a grayscale value of 45, and the threshold between the rubber powder and the matrix was at 79. These data-driven thresholds were then validated through visual inspection of the segmented slices to ensure accurate phase identification.

The final validated thresholds used for all analyses were as follows: pores (0–45), rubber powder (46–79), and cement/aggregate matrix (80–255). This segmentation process is visually represented in Figure 4. A known limitation of this approach is that the cement paste and aggregate were not segmented as separate phases.

To quantify the regularity of pore network evolution under F–T cycling, the POEI was developed. For each specimen, the change in porosity was calculated on a slice-by-slice basis for two distinct intervals: the initial damage phase (ΔP_{0-5}) and the progressive damage phase (ΔP_{0-10}).

ΔP_{0-5} = (Porosity per slice after 5 cycles) – (Porosity per slice at 0 cycles).

ΔP_{0-10} = (Porosity per slice after 10 cycles) – (Porosity per slice after 5 cycles).

These two intervals were chosen strategically. The 0–5 cycle interval captures the initial, most severe phase of damage accumulation. The subsequent 5–10 cycle interval represents the evolution of damage from an already-degraded state. By comparing the spatial patterns of pore growth in these two phases, the POEI can effectively distinguish between the expansion of existing flaws and the creation of new, independent damage sites.

The POEI is defined as the coefficient of determination (R^2) from the linear regression between these two datasets ($\Delta P_{0-5}$and ΔP_{0-10}) across the 500 slices analyzed for each specimen. The R^2 value, ranging from 0 to 1, quantifies the proportion of variance in the progressive damage that is predictable from the initial damage. A high POEI value (close to 1) indicates a strong linear relationship, signifying that the spatial pattern of damage in the second interval correlates with the initial damage – an orderly expansion of existing flaws. Conversely, a low POEI value (close to 0) indicates a weak correlation and a disordered process where new, randomly located damage is created. This analysis was performed across a continuous series of 500 slices, representing a significant vertical portion of the specimen's core, to ensure a statistically representative assessment of the internal damage distribution and its evolution.

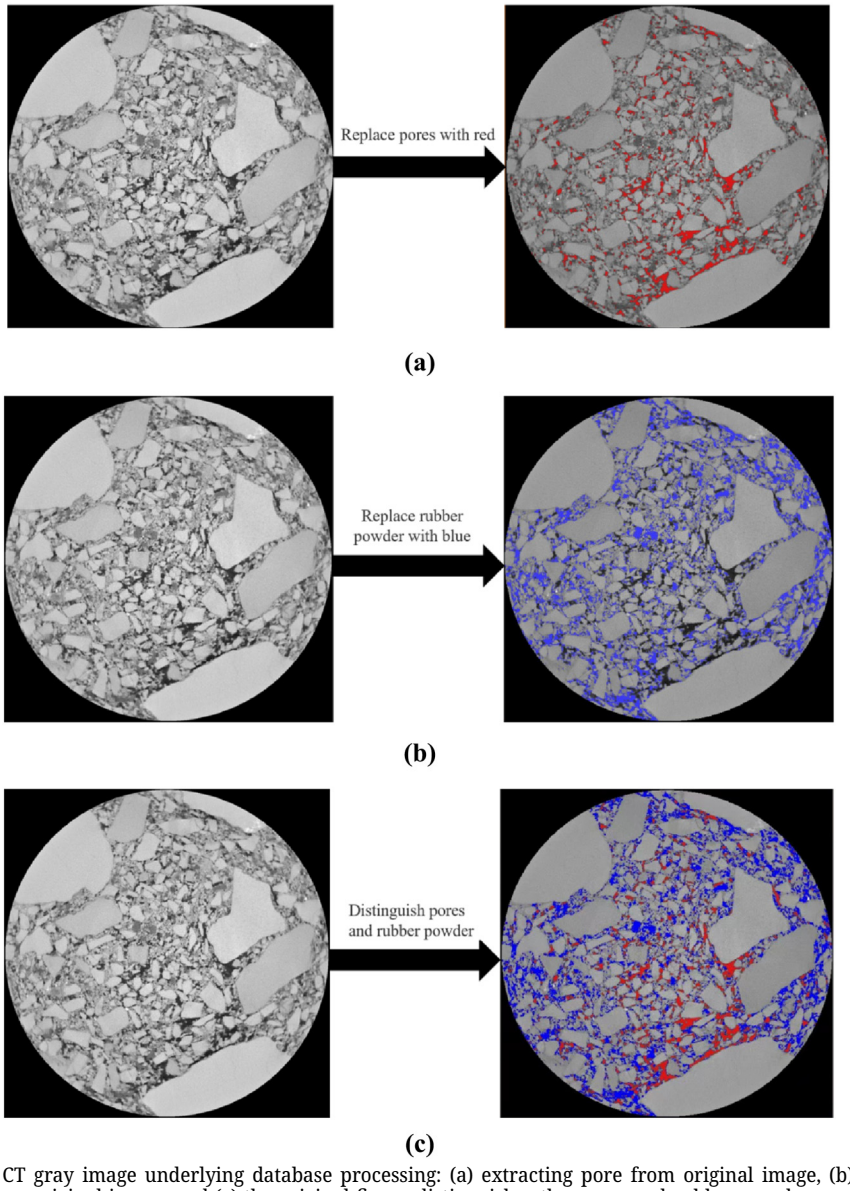

Figure 4. Industrial CT gray image underlying database processing: (a) extracting pore from original image, (b) extracting rubber powder from original image, and (c) the original figure distinguishes the pores and rubber powder.

3. Results and discussion

3.1 Unconfined compressive strength

The unconfined compressive strength decreased with increasing rubber powder content (Table 4). This is attributed to the weaker bonding between the rubber particles and the cement matrix compared to the stronger bonds within the hydrated cement and aggregate system. Nevertheless, even the material with the highest rubber content (C5R45) displayed a 7-day strength of 1.35 MPa, satisfying the minimum requirement of 1.2 MPa for railway subgrade applications.

3.2 BDR

The BDR, calculated from the strength data in Table 4, showed a non-monotonic trend: It first decreased and then increased with increasing rubber powder content (Table 5). After five F–T cycles, the BDR for the C5R45

Sample description	C5R0 (MPa)	C5R10 (Mpa)	C5R20 (Mpa)	C5R30 (Mpa)	C5R45 (Mpa)
7 days UCS	10.48	4.56	2.72	1.68	1.35
28 days UCS	11.62	7.41	5.24	2.38	1.74
5 F–T cycles UCS	10.91	4.47	3.63	2.27	1.84
10 F–T cycles UCS	10.41	4.31	3.22	2.21	1.70
15 F–T cycles UCS	9.40	4.10	3.11	2.15	1.69
20 F–T cycles UCS	8.80	4.02	2.93	2.11	1.67
30 F–T cycles UCS	8.40	3.96	2.81	2.07	1.65

Table 4. Unconfined compressive strength test results for extended F–T cycles.

material was 105.7%. This value, exceeding 100%, suggests a slight net increase in strength. This phenomenon is likely due to the continuation of cement hydration during the +20°C thaw phases. In the 28-day cured specimens, unhydrated cement particles can still react in the presence of water and favorable temperatures, leading to a strength gain that can temporarily counteract or even surpass the early-stage frost damage. After 10 cycles and continuing to 30 cycles, the BDR values decreased for all samples, but the high rubber content materials (C5R30 and C5R45) maintained significantly higher BDR values, indicating superior long-term BDR.

Sample	C5R0	C5R10	C5R20	C5R30	C5R45
5 F–T cycles BDR (%)	93.9	60.3	69.3	95.3	105.7
10 F–T cycles BDR (%)	89.5	58.2	61.5	92.4	97.7
30 F–T cycles BDR (%)	72.3	53.4	53.6	87.0	94.8

Table 5. Evaluation index of BDR.

3.3 Microscopic analysis of F–T degradation

3.3.1 Evolution of porosity under F–T cycling

The evolution of internal damage was quantified by tracking the change in porosity over the F–T cycles (Figure 5). The analysis reveals a distinct, two-stage damage progression that is highly dependent on the rubber content.

Initial Damage Stage (0–5 F–T Cycles): In the first five F–T cycles, the increase in porosity was non-monotonic with respect to rubber content. The porosity gain was most severe for the C5R10 specimen, which aligns perfectly with its low BDR. This suggests that a small amount of rubber introduces interfacial weak points that promote extensive, disordered microcracking under initial F–T stress. As rubber content increased beyond this point, the initial porosity gain decreased significantly.

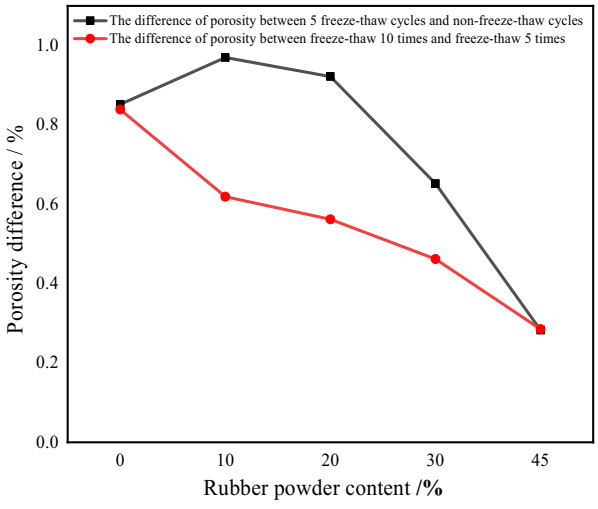

Figure 5. Change in porosity of specimens during F–T cycling. The black bars represent the porosity increase after 5 cycles (compared to 0 cycles), and the red bars represent the additional increase after 10 cycles (compared to 5 cycles).

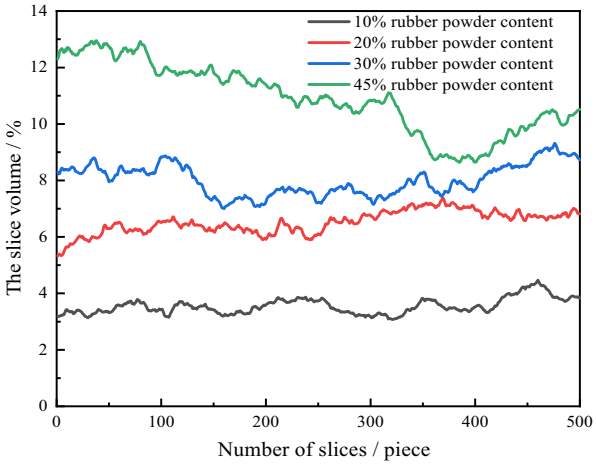

Figure 6. Volume proportion of rubber powder in each slice.

Damage Progression Stage (5–10 F–T Cycles): The analysis of damage from 5 to 10 cycles shows a different, more telling trend. The incremental increase in porosity during this period was significantly reduced with increasing rubber content. The high-content specimens (C5R30 and C5R45), which suffered less initial damage, also showed a remarkable ability to resist further degradation. Conversely, the low-content specimens continued to accumulate damage, albeit at a slower rate than in the initial stage.

This two-stage analysis provides a powerful insight: High rubber content not only mitigates the initial F–T damage but also fundamentally improves the material's long-term stability by arresting the progression of damage in subsequent cycles.

3.3.2 The change trend of pores and rubber powder in each slice

Figure 6 shows the volume ratio of rubber powder extracted from 500 slices to the total sample volume. The results show that the volume ratio of each slice in the 500 slices is relatively stable, which is consistent with the theoretical value of the volume ratio, indicating that the distribution of rubber powder in the sample is very uniform.

To quantitatively characterize the regularity of pore expansion, the relationship between initial damage (porosity change from 0 to 5 F–T cycles) and progressive damage (porosity change from 5 to 10 F–T cycles) was analyzed for each of the 500 CT slices. The results are presented as a series of scatter plots in Figure 7.

This visualization clearly illustrates the fundamental shift in the damage mechanism. For the reference specimen (C5R0), there is a moderate correlation between initial and progressive damage stages, yielding a coefficient of determination (R^2, or POEI) of 0.41. At low rubber

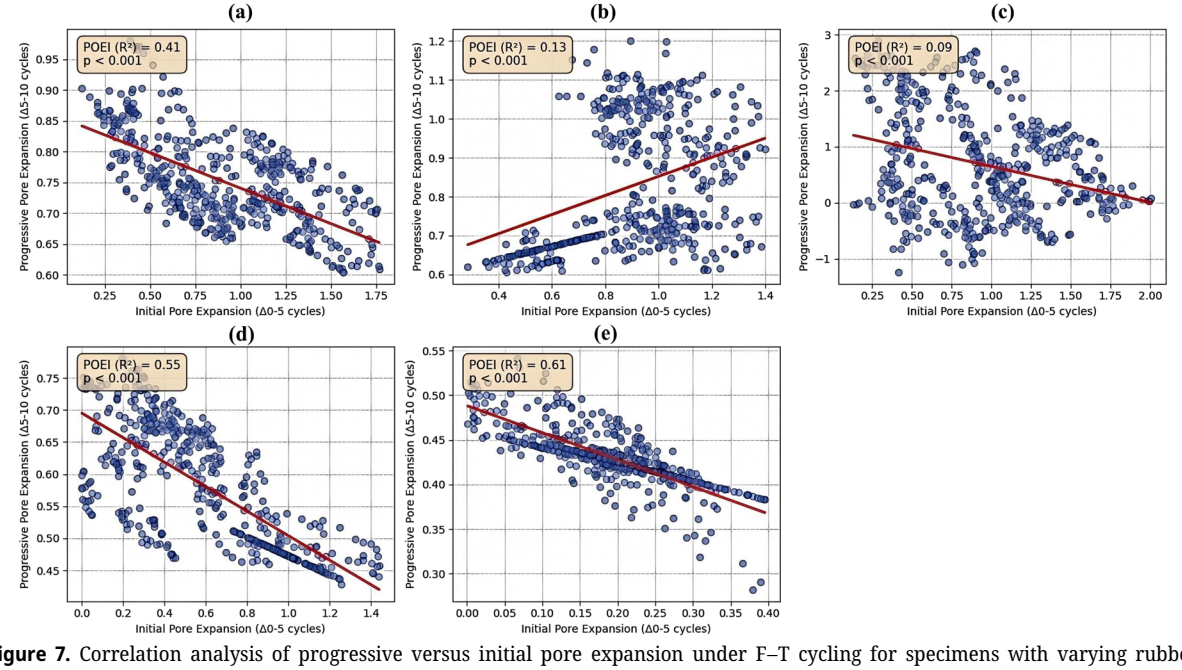

Figure 7. Correlation analysis of progressive versus initial pore expansion under F–T cycling for specimens with varying rubber

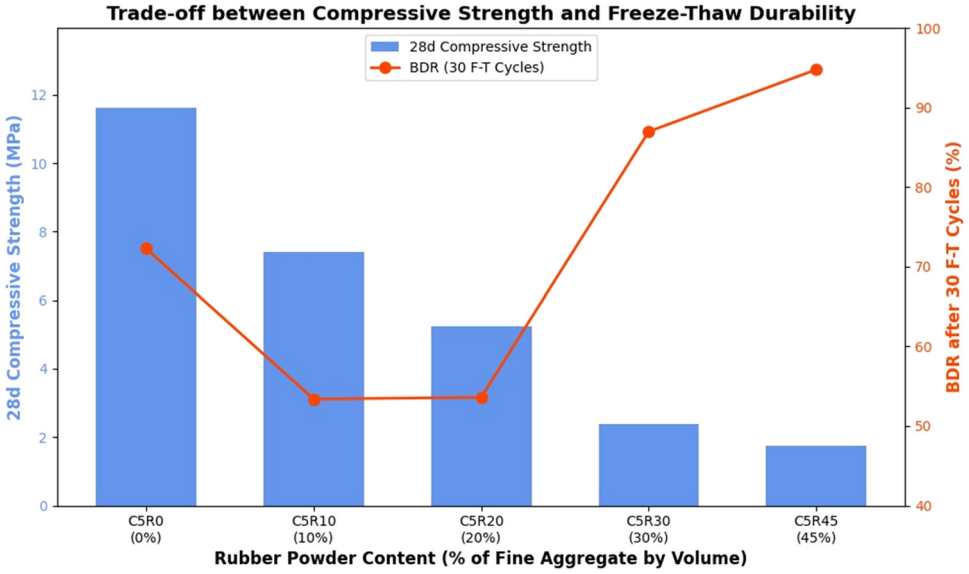

Figure 8. Comparative trend chart illustrating the trade-off between 28-day unconfined compressive strength and BDR after 30 F–T cycles.

dosages (C5R10 and C5R20), the correlation weakens significantly, reaching a minimum POEI of 0.09 for the C5R20 specimen. This low value indicates a disordered and random damage process where new microcracks form independently of initial flaws.

In stark contrast, as the rubber content increases to higher levels (C5R30 and C5R45), a strong, statistically significant linear correlation re-emerges. The points cluster more tightly around the regression line, yielding high R^2 values of 0.55 and 0.61, respectively ($p < 0.001$ for both). This demonstrates a shift back to an "ordered" damage progression, where damage accumulates primarily through the expansion of existing pores. This robust statistical and visual evidence confirms that the mode of damage evolution is fundamentally dependent on rubber content and validates the use of POEI as a key metric for frost resistance.

3.3.3 Intrinsic correlation between BDR and micropore evolution

To establish the intrinsic link between macroscopic BDR and microstructural evolution, we performed a coupled analysis. Figure 8 combines the 28-day compressive strength and the BDR after 30 F–T cycles. The chart clearly illustrates the trade-off: While strength consistently decreases with added rubber, the BDR exhibits a non-monotonic U-shaped trend,

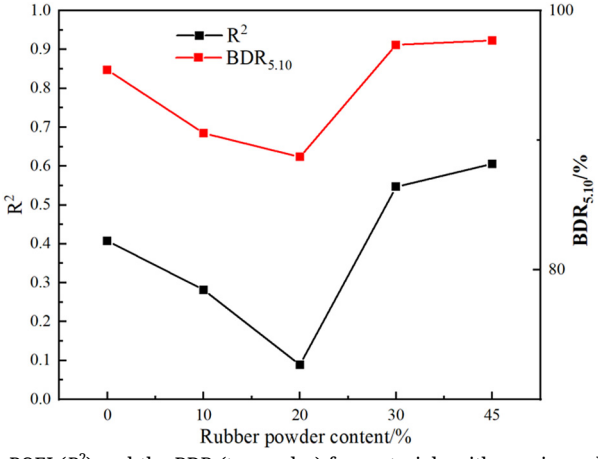

Figure 9. Correlation between the POEI (R^2) and the BDR (ten cycles) for materials with varying rubber content.

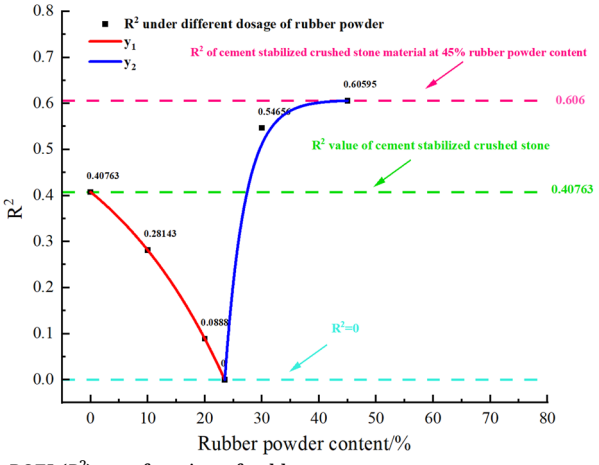

Figure 10. Quadratic model of the POEI (R^2) as a function of rubber content.

with the lowest durability observed at 10–20% rubber content and the highest durability at 45%.

3.3.4 Quantitative characterization of micro-pore evolution

This macroscopic behavior is directly explained by the microstructural damage mechanism. Figure 9 plots the POEI (R^2) against the BDR after 10 cycles. The two parameters exhibit a highly consistent trend, confirmed by a strong, statistically significant positive correlation ($p < 0.05$). This strong correlation confirms that the POEI is a powerful descriptor of BDR: A higher POEI signifies more ordered pore expansion and, consequently, superior material durability.

Based on these findings, a model correlating POEI (R^2) with rubber content was established (Figure 10). The

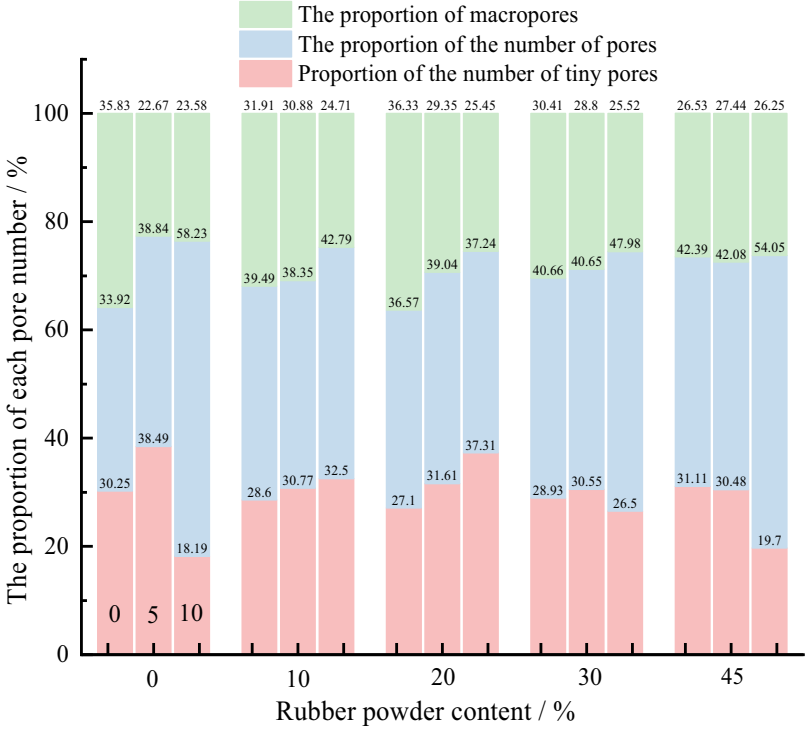

Figure 11. Change of the proportion of each pore number under the action of the F–T cycle.

model predicts a minimum POEI at a rubber content of 23.5%, aligning with the peak strength loss zone. Crucially, when rubber content exceeds 27.4%, the POEI of the modified specimens surpasses that of the traditional CSCS, demonstrating that a sufficient quantity of rubber fundamentally optimizes the pore expansion mode from disordered to ordered, thereby enhancing BDR.

3.3.5 Analysis of pore structure evolution mechanisms

To further investigate the physical mechanisms underlying the different R^2 values, a detailed analysis of the CT scanning results was conducted from three dimensions: pore number, volume, and 3D morphology.

As shown in Figure 11, the evolution patterns of pore numbers differ significantly among specimens with varying rubber content. For low-content specimens with poor BDR (e.g., 10 and 20%), F–T cycles (particularly the first 5) lead to a continuous and significant increase in the number of small pores. This indicates that new, discrete micro-cracks are constantly generated within the material under frost-heaving pressure, which corresponds to the aforementioned disordered expansion mode (low R^2). In contrast, for high-content specimens with superior BDR (e.g., 45%), the number of small pores tends to stabilize or even decrease during the F–T process, accompanied by an increase in the number of medium pores. This reveals a more stable pore evolution mode where damage is primarily manifested as the gradual expansion and interconnection of existing small pores to form medium pores, rather than the nucleation of numerous new cracks. This is a clear manifestation of ordered pore expansion (high R^2).

From the perspective of pore volume fraction (Figure 12), a decisive difference lies in the emergence of super-large pores. For this analysis, "super-large pores" (>1.00 × 10^9 μm^3 or 1 mm^3) are defined as voids whose size indicates the transition from distributed micro-damage to localized macroscopic cracks, which govern structural failure. As shown in Figure 12b, F–T cycles induce the formation and continuous development of these super-large pores in traditional CSCS and low-content rubberized specimens. However, in the high-content (45%) specimens, no super-large pores were detected throughout the entire F–T process (Figure 12a). This provides strong evidence that the high content of rubber particles effectively absorbed the frost-heaving stress, suppressed catastrophic macroscopic crack propagation, and thereby maintained the structural integrity of the material.

The 3D visualizations in Figure 13 intuitively illustrate the evolution of the pore network. While a full quantitative analysis of the network topology (e.g., using metrics like fractal dimension or connectivity index) remains a valuable direction for future work, these visualizations clearly reveal distinct differences in damage morphology. In the traditional CSCS specimens (Figure 13a and b), the pore network exhibits drastic expansion and increased connectivity between 5 and 10 F–T cycles, with smaller, isolated pores coalescing into larger, more tortuous crack networks. This signifies a widespread and interconnected damage path. In contrast, for the 30% rubber content specimen (Figure 13c and d), the changes are markedly more moderate and localized. The growth appears to be

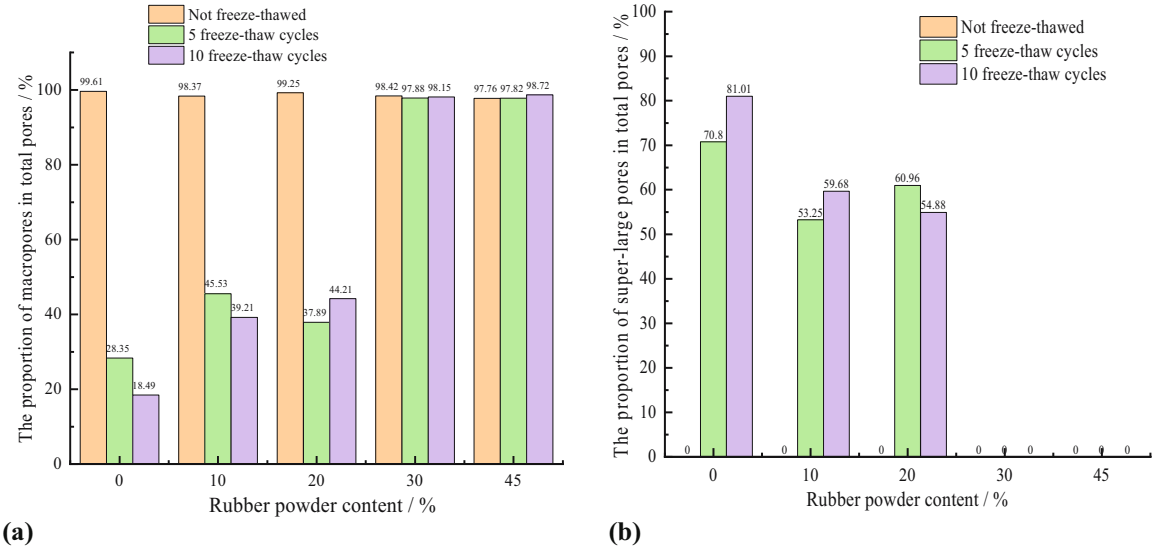

Figure 12. Change of the pore volume ratio: (a) under F–T cycles and (b) proportion of ultra-large pore volume.

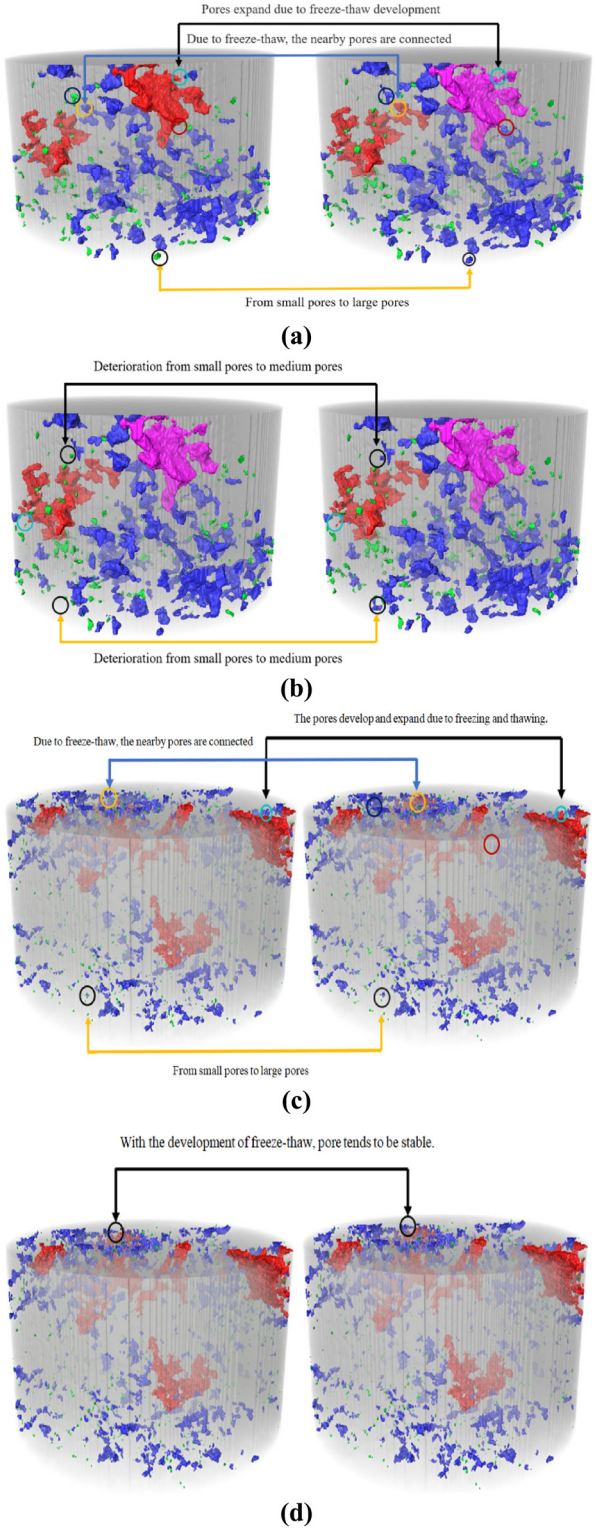

Figure 13. Changes in microstructure of CSCS before and after F–T cycles: (a) Cement stabilized macadam material five times F–T and non-F–T 3D pore diagram comparison chart. (b) Comparison of 3D pore diagram of cement stabilized macadam material between ten F–T cycles and five F–T cycles. (c) The 3D pore diagram comparison diagram of cement stabilized macadam with 30% rubber powder content after five F–T cycles and no F–T cycles. (d) The 3D pore diagram comparison of ten F–T cycles and five F–T cycles of CSCS materials with rubber powder content of 30%.

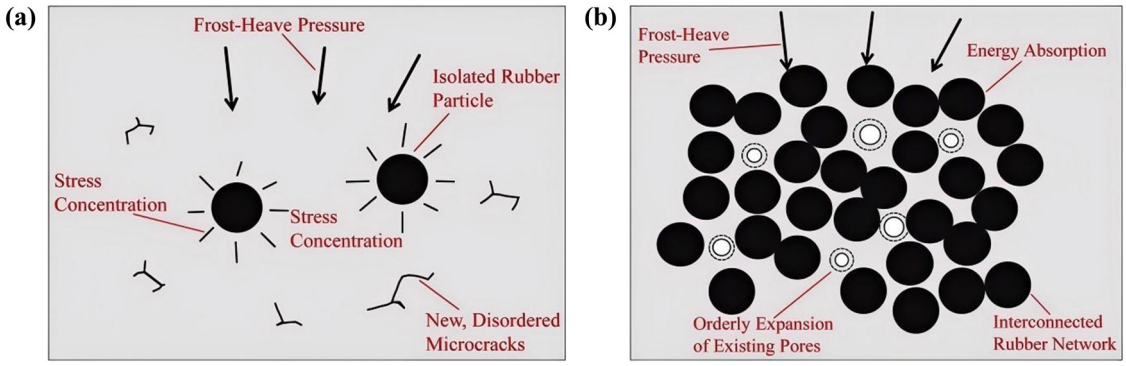

Figure 14. Schematic illustration of the proposed micro-mechanical model for F–T degradation. (a) In the low-content regime, isolated rubber particles act as stress concentrators, leading to the nucleation of new, disordered microcracks (low POEI). (b) In the high-content regime, an interconnected rubber network absorbs frost-heave energy, resulting in a more benign, orderly expansion of existing pores (high POEI).

concentrated around existing larger pores, with less formation of new, independent cracks, visually confirming the "ordered" expansion quantified by the high POEI. For instance, a future quantitative analysis using metrics like fractal dimension would likely confirm a greater increase in network complexity and tortuosity for the control specimen, corresponding to widespread damage, compared to the more stable and localized pore growth observed in the C5R30 specimen.

4. Discussion

4.1 Proposed micro-mechanical model

Based on our results, we propose a micro-mechanical model, illustrated schematically in Figure 14, to explain the non-monotonic relationship between rubber content and BDR, rooted in a shift in the microstructural damage mechanism. This model is divided into two regimes:

1. Low-Content Regime (Disordered Damage): At low concentrations (e.g., 10–20%), the isolated rubber particles act as soft inclusions within the rigid cement–aggregate matrix. Under frost pressure, these particles create weak interfacial transition zones (ITZs) that function as stress concentrators [11]. This facilitates the nucleation of new, randomly distributed microcracks throughout the matrix (Figure 14a), leading to a "disordered" damage pattern, a low POEI, and poorer BDR than even unmodified CSCS.
2. High-Content Regime (Ordered Damage): At high concentrations (e.g., ≥30%), the rubber particles are sufficiently numerous to form an interconnected, compliant network. This network fundamentally alters the material's response to frost-heaving stresses. Instead of concentrating stress, the elastic network absorbs and dissipates strain energy across the bulk material [9]. This suppresses the formation of new microcracks and accommodates stress through the gradual and uniform expansion of the existing pore structure (Figure 14b) [12]. This "ordered" damage progression, validated by a high POEI, is far less detrimental to the material's structural integrity, leading to superior BDR.

4.1.1 Implications and limitations

The central finding of this study is the quantitative link between the spatial regularity of micro-damage and macroscopic durability. While previous studies, such as those by Jie et al. [9] and Yasser et al. [12], have documented the trade-off between compressive strength and durability in rubberized materials, they often lacked a microstructural explanation for the non-monotonic behavior of BDR [10]. Our work bridges this gap by demonstrating that the orderliness of damage evolution, not just the total increase in porosity, is the critical determinant of performance. The strong correlation between the POEI and BDR validates the POEI as a powerful analytical tool and provides a new perspective for material characterization.

The implications are twofold. From an engineering perspective, they provide clear guidance for designing durable, rubber-modified materials [18]. A critical threshold (in this study, ~27.4% rubber content, where the POEI surpasses the control) must be exceeded to activate the beneficial network effect. Scientifically, the POEI offers a new paradigm for damage analysis that could be adapted for other forms of material degradation under cyclic loading.

Despite the clear findings, several limitations should be acknowledged. First, while mechanical tests were extended to 30 F–T cycles to confirm long-term performance trends,

the CT analysis was concluded at 10 cycles due to the significant time and computational resources required for high-resolution scanning and reconstruction. Therefore, longer-term microstructural studies are needed to assess the ultimate service life of these materials. Second, this study used a specific blend of rubber particle sizes; the influence of rubber gradation warrants further investigation. Finally, future work should include chemical characterization of the rubber-cement ITZ to further elucidate damage mechanisms and incorporate quantitative 3D metrics like fractal dimension to analyze pore network evolution.

5. Conclusions

This study investigated the F–T resistance of rubber-modified CSCS, leading to the following conclusions:

(1) The incorporation of rubber powder has a non-monotonic effect on BDR. Low contents (10–20% by fine aggregate volume) degraded performance, while high contents (30–45%) significantly improved it, a trend that holds for up to 30 F–T cycles.

(2) A novel microstructural parameter, the POEI, was developed and validated. A strong, statistically significant positive correlation was established between the POEI and the material's BDR. This confirms that durable materials exhibit an "orderly" damage progression (high POEI), while brittle materials fail through a "disordered" proliferation of new microcracks (low POEI).

(3) High rubber content enhances BDR by fundamentally altering the damage mechanism from disordered crack nucleation to orderly expansion of the existing pore network. This is achieved through an interconnected elastic rubber network that absorbs frost-heave energy and prevents the formation of catastrophic "super-large" pores.

(4) Considering both mechanical performance and sustainability, the C5R45 formulation represents a highly promising material for durable infrastructure in cold regions. This work establishes the POEI as a powerful framework for analyzing damage mechanisms in cementitious composites.

Funding information

This study was funded by the National Natural Science Foundation of China (No. 52172347).

Author contributions

Shuai Mao: Conceptualization, Methodology, Writing – Original Draft, Data Analysis. Yongqing Lin: Data Curation. ZuRun Yue: Supervision.

Conflict of interest statement

Authors state no conflict of interest.

Data availability statement

All data generated or analyzed during this study are fully included within the manuscript.

References

[1] Tian, X., Guo, L., Development status of recycling and resource utilization of waste tires, Prog. Mater. China, 2022, 41(1): 22–29 + 66–67

[2] Han, X., The main index of transportation industry in the fourth quarter has an obvious upward trend, People's Dly. (in Chinese), 2024. doi: 10.28655/n.cnki.nrmrb.2024.016668

[3] Cai, D., Ye, Y., Lou, L., Shi, Y., Pang, S., Research status and development trend of asphalt concrete structure of high-speed railway roadbed, J. Railw. Sci. (in Chinese), 2022, 44(10): 112–122. doi: 10.3969/j.issn.1001-8360.2022.10.015

[4] Ye, Y., Cai, D., Zhang, Q., Wei, S., Yan, H., Geng, L., Current status and development trend of design method for high-speed railway subgrade bed structure, China Railw. Sci., 2021, 42(3): 1–12

[5] Zhang, J., Jie, S., Yue, Z., Mao, S., Zuo, Z., Analysis of dynamic characteristics of cement stabilized macadam mixed with rubber powder in high-speed railway subgrade bed, Sci. Technol. Eng. (in Chinese), 2023, 23(16): 7064–7073

[6] Sun, X., Wu, X., Zhao, G., Yan, Z., Investigation on the micromechanical damage mechanism of cement-stabilized macadam after multiple freeze-thaw cycles, Front. Mater., 2025, 11: 1479306. doi: 10.3389/fmats.2024.1479306

[7] Jie, S., Yue, Z., Sun, Z., Zhang, H., Hu, T., Sun, T., et al., Frost resistance and mechanical degradation characteristics of cement-stabilized macadam under the

long-term freezing–thawing cycles, Constr. Build. Mater., 2022, 347: 128545. doi: 10.1016/j.conbuildmat.2022.128545

[8] Jie, S., Yue, Z., Sun, T., Yang, Z., Zhang, H., Freeze-thaw deterioration test and model study of cement stabilized gravel bed, Sci. Technol. Eng. (in Chinese), 2021, 21(8): 3318–3324

[9] Jie, S.L., Mao, S., Yue, Z.R., Sun, Z.Q., Sun, T.C., Hu, T.F., et al., Frost resistance and mechanical characteristics of cement-stabilized macadam mixed with rubber powder, J. Mater. Civ. Eng., 2023, 35(7). doi: 10.1061/jmcee7.Mteng-14871

[10] Liu, H., Qian, J., Jin, C., Qian, X., Investigation of mechanical performance and voids structure of cement-stabilised macadam under freeze-thaw actions, Int. J. Pavement Eng., 2023, 24(1): 2225120. doi: 10.1080/10298436.2023.2225120

[11] Liang, C., Wang, Y., Tan, G., Zhang, L., Zhang, Y., Yu, Z., Analysis of internal structure of cement-stabilized macadam based on industrial CT scanning, Adv. Mater. Sci. Eng., 2020, 2020(1): 5265243. doi: 10.1155/2020/5265243

[12] Yasser, N., Abdelrahman, A., Kohail, M., Moustafa, A., Experimental investigation of durability properties of rubberized concrete, Ain Shams Eng. J., 2023, 14(6). doi: 10.1016/j.asej.2022.102111

[13] Zhang, J., Wu, M., FitzGerald, P., Araujo, S., De Man, B., Development and tuning of models for accurate simulation of CT spatial resolution using CatSim, Phys. Med. Biol., 2024, 69(4): 045014

[14] Sun, B.W., Xu, T.L., Zhang, H.W., Li, Y., Huang, X., Qi, L., et al., Analysis of alkali leaching mechanism on as-built cement concrete bridge deck pavement: View from the perspective of mesostructure characteristics, Constr. Build. Mater., 2023, 409: 134054. doi: 10.1016/j.conbuildmat.2023.134054

[15] Tu, Y.L., Long, H., Fang, Z., Chai, H.J., Liu, X.R., Zhang, L.Z., et al., A new numerical method for constructing the three-dimensional microstructure of S-RM using digital image processing technology, Granul. Matter., 2024, 26(1). doi: 10.1007/s10035-023-01393-0

[16] Huang, M., Xu, K., Liu, Z.J., Xu, C.S., Cui, M.J., Effect of drying-wetting cycles on pore characteristics and mechanical properties of enzyme-induced carbonate precipitation-reinforced sea sand, J. Rock. Mech. Geotech. Eng., 2024, 16(1): 291–302. doi: 10.1016/j.jrmge.2022.12.032

[17] State Railway Administration of the People's Republic of China, Codes for design of high speed railway, People's Communications Press, Beijing, 2014. TB10621-2014

[18] Yan, H., Zhao, G., Cai, D., Wang, Z., Zhang, Q., Yao, J., Research on anti-frost heaving structure of permeable subgrade bed on high speed railway, Railw. Eng., 2015, 5: 98–102

[19] Ding, J.S., Research and implementation of algorithms in FPGA-based image processing system, Hefei University of Technology, Hefei, China, 2015

[20] Gonzalez, R.C., Digital image processing, Publishing House of Electronics Industry, Beijing, 2011, pp. 1–8

[21] Meng, Q.L., Introduction to design standards and explanations for railway structures, Railw. Build., 2007, 10: 102